# Time-resolved loads on a lab-scale axial-flow turbine with passive adaptive blades

K. Van Ness, C. Crisp, B. Polagye - University of Washington

March 2024

**Abstract**

Passive adaptive blades for axial-flow marine current turbines offer the potential for blade load reductions without introducing failure modes inherent to active pitch mechanisms. To support the development of simulation tools for passive adaptive turbine rotors, an experimental data set from a laboratory-scale axial-flow turbine with passive adaptive blades is provided. The blades were fabricated with unidirectional off-axis carbon fiber, resulting in a coupling between flapwise deflection and spanwise twisting. The 0.45-meter diameter turbine was tested in an open-channel, recirculating flume at three flow speeds ($Re = 2.7 - 3.6 \cdot 10^5$) over tip-speed ratios 2-8. Blade and rotor loads were measured at 1 kHz using six-axis force/torque sensors at the root of a blade and on the drive shaft in the rotor hub, while deflection and twist at the blade tip were tracked using a high-speed camera. Frequency analysis of the blade loads revealed no evidence of flutter instability, with dominant frequencies identified only at the blade passing frequency and associated harmonics.

## 1 Introduction

To support the Blue Economy [1], research and development that targets improving the cost and reliability of marine energy technologies at the kW-scale and smaller is required. Utility-scale deployments around the world have demonstrated the viability of generating electricity from ocean, river, and tidal currents [2], but component failure, curtailment, and underperformance are still common [3]. One strategy for increasing reliability and decreasing cost of axial-flow marine current turbines is with passive adaptive blade technology. Passive adaptive blades are designed to elastically deform in response to above-rated or unsteady flow conditions. By using a layup of anisotropic composite materials, bending and twisting deformations are coupled such that when the blades bend under increased load, they simultaneously twist to shed power and load (Fig. 1). In the wind industry, an active blade pitch control method is conventionally used, but due to the increased risk of failure associated with active pitch mechanisms in underwater environments, a standard has not yet emerged for marine current turbines. To date, both fixed- and variable-pitch turbines have been used in full-scale deployments [4].

In passive adaptive blade design, simulation tools are valuable for optimizing mechanical properties and blade shape through variations in composite type, fiber orientation, ply count, and other material options. While some numerical studies have explored analysis and optimizations of passive adaptive blade designs for wind turbines [5, 6, 7], few studies explore applications for marine current turbines. Those that do typically use fluid-structure interaction models combining a finite element model (FEM) with blade element momentum thoery (BEMT) which are validated separately [8, 9, 10], without further validation of a fully-coupled FEM-BEMT model. Furthermore, time-resolved experimental data for passive adaptive turbine blades has not been available to rigorously validate numerical models which could capture high-frequency behavior such as flutter instabilities [11]. To address this gap, this report provides an experimental data set from a laboratory-scale axial-flow turbine with passive adaptive blades that could be used to validate such a numerical model.

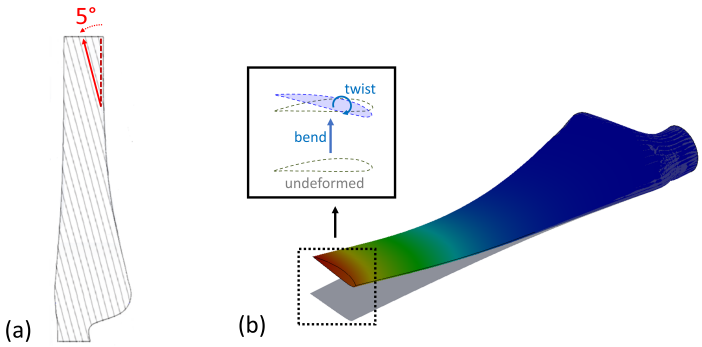


Figure 1: (a) Unidirectional, off-axis fibers result in anisotropic blade properties and (b) a coupling between flapwise deflection and spanwise twisting.

# 2 Methods

## 2.1 Turbine instrumentation & facility

A three-bladed, variable-speed axial-flow turbine, identical to the one used in [12, 13], was used to test passive adaptive turbine blades in the Alice C. Tyler Flume at the University of Washington. The 0.45-meter diameter, variable-speed turbine and its instrumentation is shown in Fig. 2. A six-axis load cell (Mini45, ATI Industrial Automation) was installed on the drive shaft of the turbine, in the rotor hub, to measure thrust and torque on the rotor, while a second six-axis load cell (Nano25, ATI Industrial Automation) was installed at the root of a single blade (referenced herein as the "key blade") to measure flapwise forces and root bending moments experienced by an individual blade. Load cell coordinate systems are defined in Fig. 3. The turbine rotor was connected to a 5:1 gearbox (PV23, Parker Hannefin) and double-shaft stepper motor (LV233, Parker Hannefin), with an optical encoder (ZAA, Applied Motion Products) mounted on the rear shaft to track azimuthal position of the key blade. Power and communication signals were transmitted to the rotating hub through a slip ring. Sampling rates on the load cells and encoder were 1 kHz and 50 Hz, respectively. Azimuthal position was linearly interpolated between encoder measurements to determine a position for every load cell measurement. The data acquisition script was written in C++ using a CAN bus protocol to communicate with the load cells and RS485 protocol with the stepper motor and encoder. The new data acquisition software in C++ (previously written in MATLAB) is the primary difference from previous flume experiments with this turbine [12, 13] and increased acquisition rates by two orders of magnitude.

Flow speed through the recirculating, open-channel flume was controlled by two pumps with a variable frequency drive. The test section was 0.76-meter wide and fill height was adjusted to obtain a dynamic depth of 0.6 meters for all experiments. This resulted in a geometric blockage ratio of 35 %, which increases power and thrust relative to unconfined conditions [14]. Pump frequencies were held constant during data acquisition to maintain 0.6, 0.7, and 0.8 m/s inflow velocities. Turbulence intensities are relatively low (2.0-4.4%) for velocities in this range [12]. Free-stream velocity, $U$, was measured 1 m downstream of the test section entry (i.e., 154 cm or 3.4 turbine diameters upstream of the rotor plane) using an acoustic Doppler velocimeter (ADV, Nortek Vector) sampling at 16 Hz. Water temperature was maintained at 20°C for all experiments.

We define a diameter-based Reynolds number as

$$Re_D = \frac{UD}{\nu}, \tag{1}$$

where $D$ is the turbine diameter and $\nu$ is the kinematic viscosity of water at 20°C. By this definition, the three test cases in 0.6, 0.7, and 0.8 m/s correspond to Reynolds numbers of $2.7 \cdot 10^5$, $3.1 \cdot 10^5$, and $3.6 \cdot 10^5$. Previous experiments with rigid blades of the same geometry demonstrated Reynolds-independence in flow

speeds above 0.7 m/s at 20°C, however even flow speeds as low as 0.6 m/s resulted in power and thrust coefficients within 5% of the Reynolds-independent values [12], suggesting that the the results presented here are largely independent of changes in viscosity.

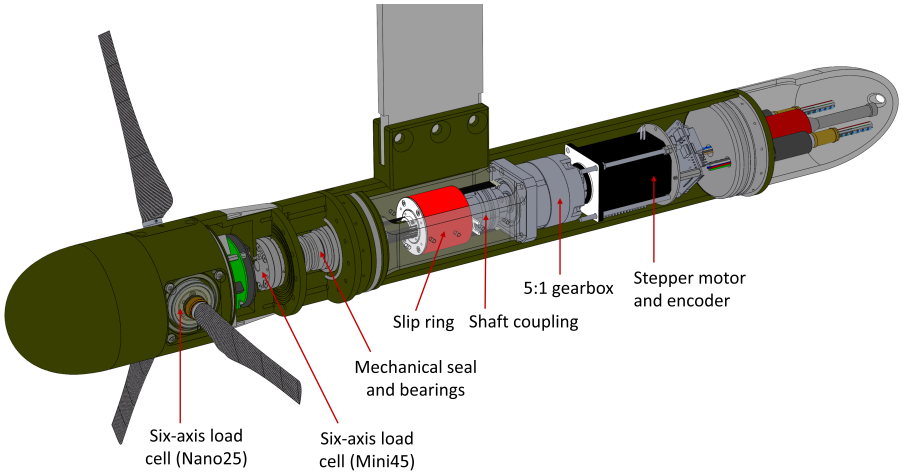


Figure 2: CAD model of turbine and instrumentation.

## 2.2 Blade design and fabrication

The passive adaptive blades used for these experiments were fabricated with a 5° off-axis fiber orientation such that the blade twisted towards the "feather" position under load, decreasing the angle of attack. Blade geometry, based on the NACA-44 airfoil series, is described in Table 1, and step-by-step details of the blade fabrication process are described in [13]. The blades are composed of a central carbon fiber spar cast in a semi-rigid polyurethane. The carbon fiber provides the bend-twist coupling while the polyurethane provides the hydrodynamic blade shape. The final composite blade is shown in Fig. 4, and properties of the carbon fiber are listed in Table 2. The longitudinal Young's modulus, $E_1$, is the only manufacturer-specified property [15]. The remaining properties are approximated from a material property data report by the National Institute for Aviation Research (NIAR) that tests the same Hexcel matrix reinforced with a similar Hexcel carbon fiber [16].

Static mechanical testing was also performed, during which the blade was loaded at the tip while the deflection and twist were measured using laser displacement sensors. An actuator provided the load and the reaction force/torque was measured at the blade root with a six-axis load cell. These methods are detailed in [13], and the results are shown in Fig. 5. Loads were applied at the quarter-chord to determine the bending stiffness (Fig. 5a), but this did not produce measurable torque in the load cell so loads were applied at the trailing edge to determine the torsional stiffness (Fig. 5b). Results indicate similar, but not identical, mechanical properties for each blade as a consequence of slight differences in the blade-to-blade fabrication process.

## 2.3 Characteristic performance and loading

We define a coefficient of power, $C_P$, as the ratio of the turbine's mechanical power output relative to the kinetic power available in the inflow across the rotor swept area:

$$C_P = \frac{\langle Q_{z,h}\omega \rangle}{0.5\rho A \langle U^3 \rangle} \tag{2}$$

where $Q_{z,h}$ is the torque measured by the six-axis load cell on the driveshaft, $\omega$ is the rotational speed commanded by the stepper motor and verified by the encoder, $\rho$ is water density, and $A$ is the rotor swept

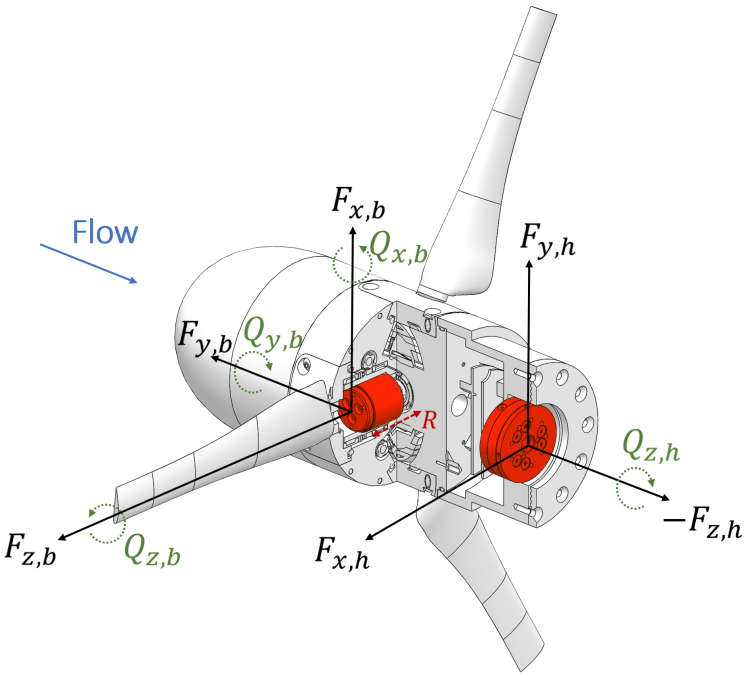


Figure 3: Blade and drive shaft load cell coordinate systems.

area. We define a coefficient of thrust, $C_T$, as the streamwise force, $T$, acting on the turbine relative to the dynamic pressure force across the rotor swept area:

$$C_T = \frac{\langle F_{z,h} \rangle}{0.5\rho A \langle U^2 \rangle} \tag{3}$$

where $F_{z,h}$ is also measured by the six-axis load cell on the driveshaft (Fig. 3). Time-averaged values of $C_P$ and $C_T$ are calculated over a 65-second interval for each of a range of tip-speed ratios, $\lambda$, defined as:

$$\lambda = \frac{\omega R}{\langle U \rangle} \tag{4}$$

where $R$ is the turbine radius. We note that during the 0.6 m/s inflow case, only a 45-second interval was used due to an inadvertent error introduced during the experimental procedure. To correct for azimuthal variations in static force and torque measured by the load cell, tare measurements were collected at 12 equidistant azimuthal positions. During post-processing, instantaneous force and torque measurements were corrected using a spline interpolation of the tare values.

## 2.4 Blade deformation

To remotely measure blade deformation at the tip during turbine operation, a high speed camera (Vision Research, Phantom c641) was positioned below the glass test section of the flume to capture the location and orientation of each passing blade tip at a frame rate of 4300 fps and a resolution of 1024x1024 pixels. Blade tips were coated with a reflective chrome paint to increase contrast. Video of at least 45 blade passages was recorded at each tip-speed ratio and manually sorted by blade number (1, 2, or 3) according to marks on the blade tip. During image processing, the frame that most closely aligns the blade in the center of the camera view was compared to an image of the unloaded blade to calculate deflection and twist at the blade tip. Blades sometimes passed without triggering a recording on the camera, so there are not an equal number of deformation measurements for all three blades. Additional details on these methods are described in [13].

Table 1: Blade geometry, where $r$ is the local radius, $R$ is the turbine radius, $c$ is the local chord, and $t$ is the local thickness. Pre-twist is defined as the relative angle between the local chord and the plane of rotation, where positive angles indicate the leading edge is upstream of the rotor plane.

| $r/R$ | $c/r$ | $t/c$ | Pre-Twist(°) |
|---|---|---|---|
| 0.244 | 0.318 | 1.000 | 14.60 |
| 0.262 | 0.303 | 1.000 | 14.60 |
| 0.300 | 0.271 | 0.963 | 14.60 |
| 0.330 | 0.484 | 0.350 | 14.56 |
| 0.355 | 0.554 | 0.223 | 14.02 |
| 0.381 | 0.499 | 0.208 | 13.01 |
| 0.410 | 0.438 | 0.201 | 11.46 |
| 0.441 | 0.385 | 0.193 | 10.03 |
| 0.474 | 0.334 | 0.185 | 9.32 |
| 0.510 | 0.288 | 0.177 | 8.48 |
| 0.548 | 0.247 | 0.167 | 7.81 |
| 0.590 | 0.212 | 0.167 | 7.05 |
| 0.635 | 0.183 | 0.159 | 6.25 |
| 0.684 | 0.159 | 0.147 | 5.69 |
| 0.736 | 0.140 | 0.147 | 5.21 |
| 0.790 | 0.126 | 0.148 | 4.66 |
| 0.902 | 0.106 | 0.149 | 3.66 |
| 0.959 | 0.100 | 0.150 | 3.17 |
| 1.000 | 0.096 | 0.154 | 3.31 |

Table 2: Approximate material properties for HexPly 8552 epoxy matrix reinforced with HexTow AS4, 12K carbon fiber used for blade spars [16, 15].

| Material Property | Value |
|---|---|
| Longitudinal Young's modulus (parallel to fibers), $E_1$ | 135 GPa |
| Transverse Young's modulus (perpendicular to fibers), $E_2$ | 9.72 GPa |
| Shear modulus, $G_{12}$ | 4.69 GPa |
| Poisson's Ratio, $\nu_{12}$ | 0.356 |

## 2.5 Blade center of pressure

We approximate the spanwise and chordwise center of pressure on the blade using force and torque measurements from the six-axis load cell installed at the blade root of the key blade. Referring to the coordinate system of the blade load cell defined in Fig. 3, we relate the pitching moment, $Q_{z,b}$, to the thrust force on the blade, $F_{y,b}$:

$$\langle Q_{z,b} \rangle = \langle F_{y,b} \rangle R_{PM}, \tag{5}$$

where $R_{PM}$ is the pitching moment arm, i.e., the chordwise distance between the pitching axis (located at the quarter-chord) and the center of pressure on the blade (Fig. 6). $\langle Q_{z,b} \rangle$ and $\langle F_{y,b} \rangle$ are direct measurements from the blade load cell, averaged over the entire time series at each tip-speed ratio. We similarly relate the flapwise blade root bending moment, $Q_{x,b}$, to the thrust force on the blade:

$$\langle Q_{x,b} \rangle = \langle F_{y,b} \rangle R_{FBM}, \tag{6}$$

where $R_{FBM}$ is the flapwise bending moment arm, i.e., the spanwise distance between the sensor head of the load cell and the center of pressure on the blade. To report the center of pressure as the span-wise distance, $z$, from the blade root, we subtract the distance between the sensor head and blade root from $R_{FBM}$ (Fig.

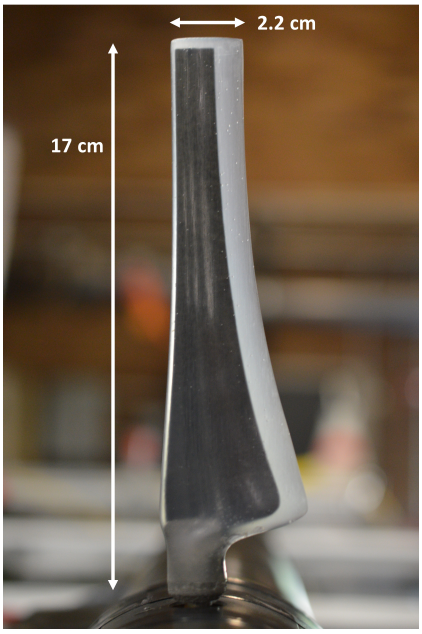


Figure 4: Flexible, composite blades composed of a carbon fiber spar (black), to provide the desired bend-twist coupling, and a semi-rigid polyurethane outer (translucent white-grey) to provide the desired blade geometry and hydrodynamic behavior.

6). Uncertainty in the center of pressure calculations is introduced through the spanwise variation in twist inherent to the blade geometry and the passive twist behavior observed during a test; Eqns 5 and 6 assume $F_{y,b}$ is perpendicular to the chord, which is an appropriate assumption for small changes in twist. Additional uncertainty is introduced through the blade load cell measurements which are biased low by a shaft seal at the root of the blade, between the blade and the load cell. From static testing, we estimate approximately 5% of the blade loads are taken by the seal and not seen by the load cell.

# 3 Results & Discussion

## 3.1 Turbine performance and blade deformation

Fig. 7 shows power and thrust coefficients for three flow speed cases: 0.6, 0.7, and 0.8 m/s. The peak power coefficients are similar across all three cases at 48-49%. These are augmented by blockage relative to their unconfined value. We observe two relatively subtle differences in the power coefficients as a function of inflow velocity: (1) an increase in power at low tip-speed ratios and (2) a decrease in power at high tip-speed ratios. Since higher flow speeds increase the flapwise blade load, a larger twist angle (i.e., smaller angle of attack) is induced (Fig. 8b), both delaying stall at low tip-speed ratios and shedding power at high tip-speed ratios. However, we note that the experimental uncertainty, quantified by the interquartile range of $C_P$, increases with tip-speed ratio, and that the differences in power coefficients with inflow velocity at high tip-speed ratios fall mostly within the interquartile range at these operating points (Fig. 7a).

The differences in thrust coefficients across each inflow case are more pronounced, with peak $C_T$ at 0.7 and 0.8 m/s decreasing by 5% and 12%, respectively, from the 0.6 m/s case. For comparison, $C_T$ for a rigid blade would be unaffected by $U$ in a Reynolds-independent regime or increase in a Reynolds-dependent regime. It is important to note that while the normalized thrust load, $C_T$, on the passive adaptive blade decreases when $U$ increases (for $\lambda > 4.2$), the absolute thrust load, $F_{z,h}$ is still increasing with $U$ because $C_T$ is declining at a rate less than $U^2$. This explains the corresponding increases in deflection and twist observed in Fig. 8.

Fig. 8 shows the deflection and change in twist at the blade tip for all three blades, including measure-

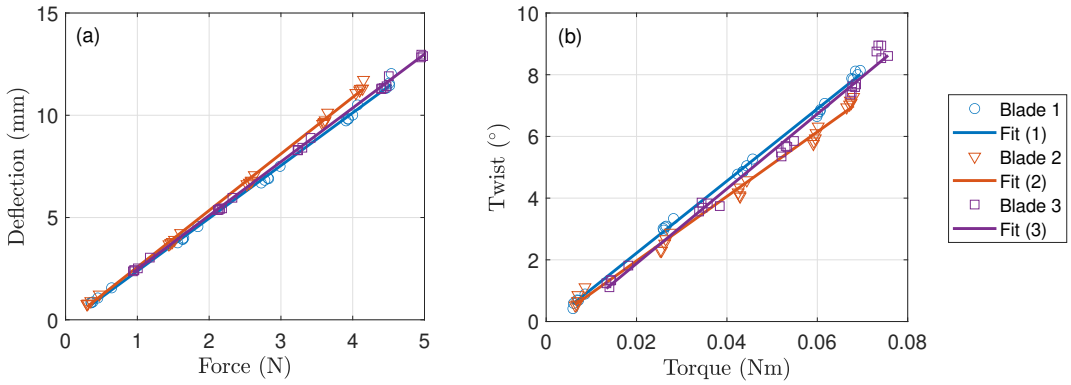


Figure 5: Each blade underwent static mechanical testing to determine bending and torsional stiffness. Results show (a) tip deflection as a function of the applied force and (b) tip twist as a function of the applied torque.

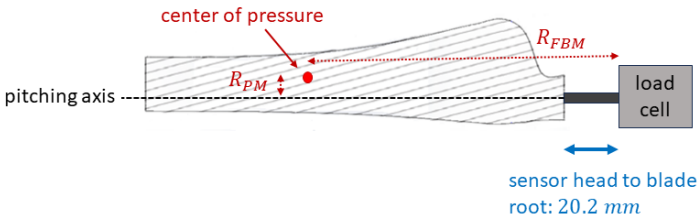


Figure 6: Force and torque measured from the blade load cell are used to calculate the pitching moment arm, $R_{PM}$, and the flapwise bending moment arm, $R_{FBM}$. We further define $R_{PM}$ as the distance between the pitching axis and the chord-wise center of pressure, while $R_{FBM}$ is the distance between the sensor head of the blade load cell and the span-wise center of pressure.

ments from individual blade passages and the median at each tip speed ratio. We observe an increase in deflection and twist with an increase in $U$ over most tip-speed ratios. We also observe a linear increase in twist with tip-speed ratio for $\lambda > 4$, whereas deflection peaks in the middle of the tip-speed ratio range and then starts to decrease at high tip-speed ratios, similar to results in [17, 18]. To explain this result, we turn to the center of pressure calculations shown in Fig. 9. We see that as the tip-speed ratio increases, the center of pressure moves towards the trailing edge, producing a larger pitching moment and greater twist deformation, thereby reducing flapwise blade loads and blade deflection at sufficiently high tip-speed ratios. The peak in $C_T$ roughly aligns with the peak $\Delta\delta_{tip}$, which further supports this explanation of blade behavior.

Significant differences in the deformation observed between each blade 1-3 (Fig. 8) are likely explained by blade-to-blade variations in mechanical properties introduced during blade fabrication. For example, from Blade 2 we measured up to 3° less twist during flume testing than Blades 1 and 3 (Fig. 8b), and Fig. 5b shows that Blade 2 also experienced less twist compared to Blades 1 and 3 during static mechanical testing. These differences are substantially greater than cycle-to-cycle variation in tip deflection and twist, indicating the benefits of a more consistent manufacturing process for future experiments.

## 3.2 Time-resolved loads

Time-resolved blade and hub loads, ranging from 230-1000 samples per revolution depending on rotation rate, are provided in this data set to serve as validation data for time-resolved or time-averaged models. This includes rotor thrust, rotor torque, flapwise blade force, edgewise blade force, flapwise blade root bending

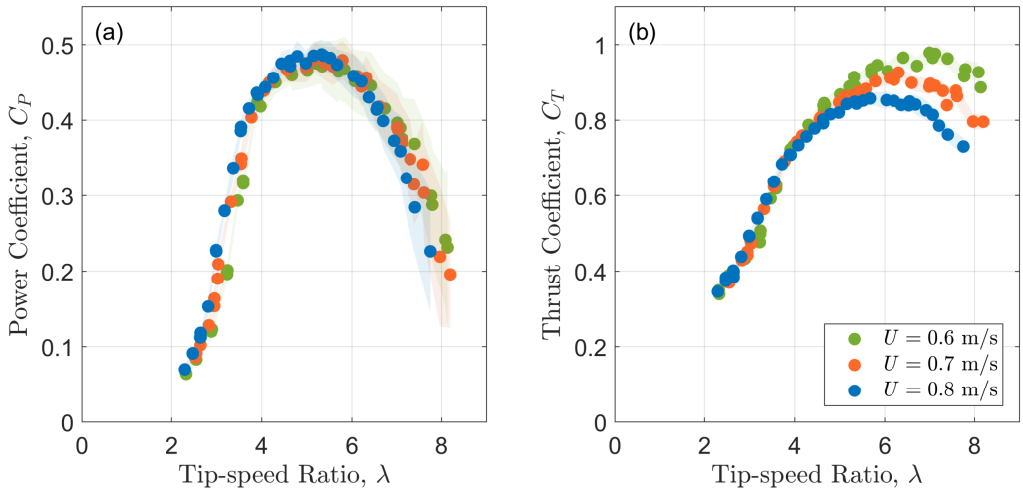


Figure 7: Coefficients of (a) power and (b) thrust as a function of tip-speed ratio in 0.6-0.8 m/s flow. Shaded regions represent the interquartile range.

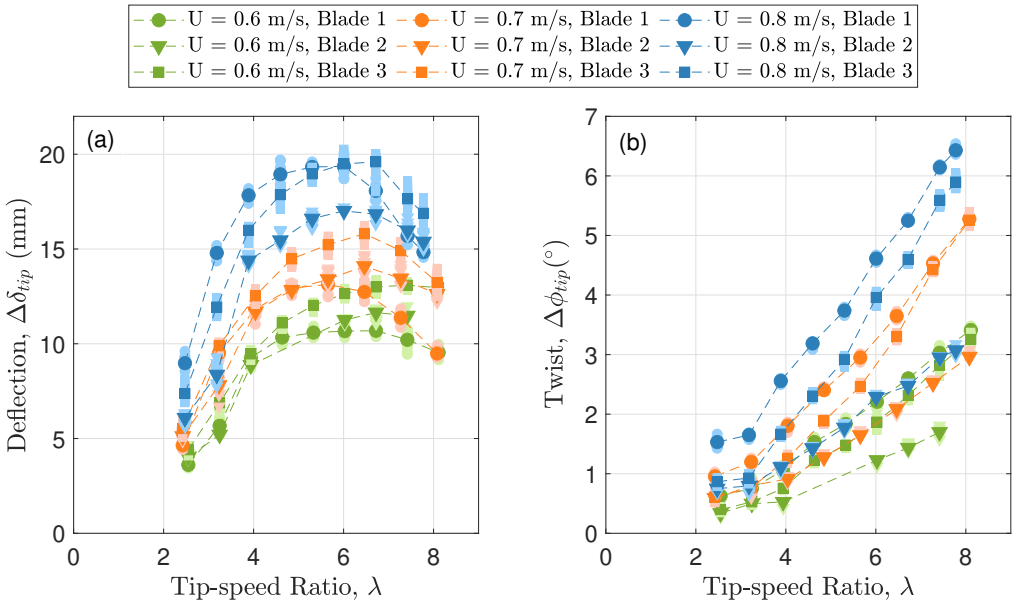


Figure 8: Change in (a) deflection and (b) twist at the blade tip as a function of tip-speed ratio. Light colored markers represent measurements from individual blade passages while the darker colored markers represent the median.

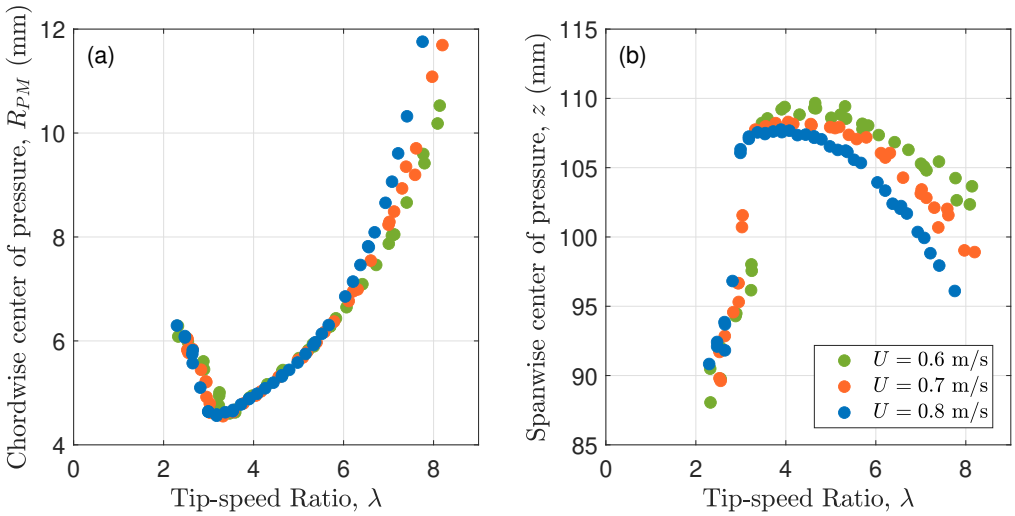


Figure 9: Calculated (a) chordwise and (b) spanwise center of pressure as a function of tip-speed ratio. The chordwise location is relative to the pitching axis (located at the quarter-chord), where positive values are towards the trailing edge. The spanwise location is relative to the blade root, where 170 mm is the blade tip.

moment (RBM), edgewise RBM, and pitching moment. Sample time series over a few seconds are shown in Fig. 10. As previously mentioned, the full time series are 65-seconds long for the 0.7 and 0.8 m/s cases and 45-seconds long for the 0.6 m/s case (due to an inadvertent error introduced during the experimental procedure). The measurements of tip deflection and tip twist from the high-speed camera are not time-resolved and are only meant to represent steady-state blade deformation.

A frequency analysis of the flapwise RBM is shown in Fig. 11. This sample is from the 0.8 m/s inflow case and 6 rotation rates are shown: 1.5-4.0 rps. Dominant frequencies are present at the blade passing rate and associated harmonics, shown with the dashed lines. No other dominant frequencies are present, suggesting that flutter is relatively negligible. Similar results are obtained for flapwise blade force and edgewise force/torque at the same and other rotation rates and inflow cases.

# 4 Summary and future work

In this work, a 0.45-diameter axial-flow turbine equipped with flexible, passive adaptive turbine blades underwent flume testing in three flow speeds, 0.6-0.8 m/s ($Re = 2.7 - 3.6 \cdot 10^5$). Peak power coefficients remained constant across all three flow speed cases, while peak $C_T$ at 0.7 m/s and 0.8 m/s decreased by 5% and 12%, respectively, from the 0.6 m/s case as a consequence of blade deformation and the tailored bend-twist coupling. Blade deflection was observed to increase and then decrease with $C_T$ while twist increased linearly with tip-speed ratio, likely due to changes in the chordwise center of pressure on the blade, which moved towards the trailing edge as tip-speed ratio increased. No evidence of flutter was found in the frequency analysis of the blade loads, which only showed dominant frequencies at the blade passing frequency and associated harmonics.

The primary purpose of this work was to produce experimental data that could be used to validate numerical models. A fluid-structure interaction (FSI) model validated by the provided data set would be a valuable tool, allowing for a more thorough investigation into the behavior and design optimization of passive adaptive blades. Future work could include designing a blade with intentional flutter characteristics to generate data that could validate this aspect of a hydroelastic FSI model. With an optimal design, these blades have the potential to reduce blade loads in extreme or unsteady flow conditions without impacting power output under normal operating conditions, which can lead to reduced technology costs.

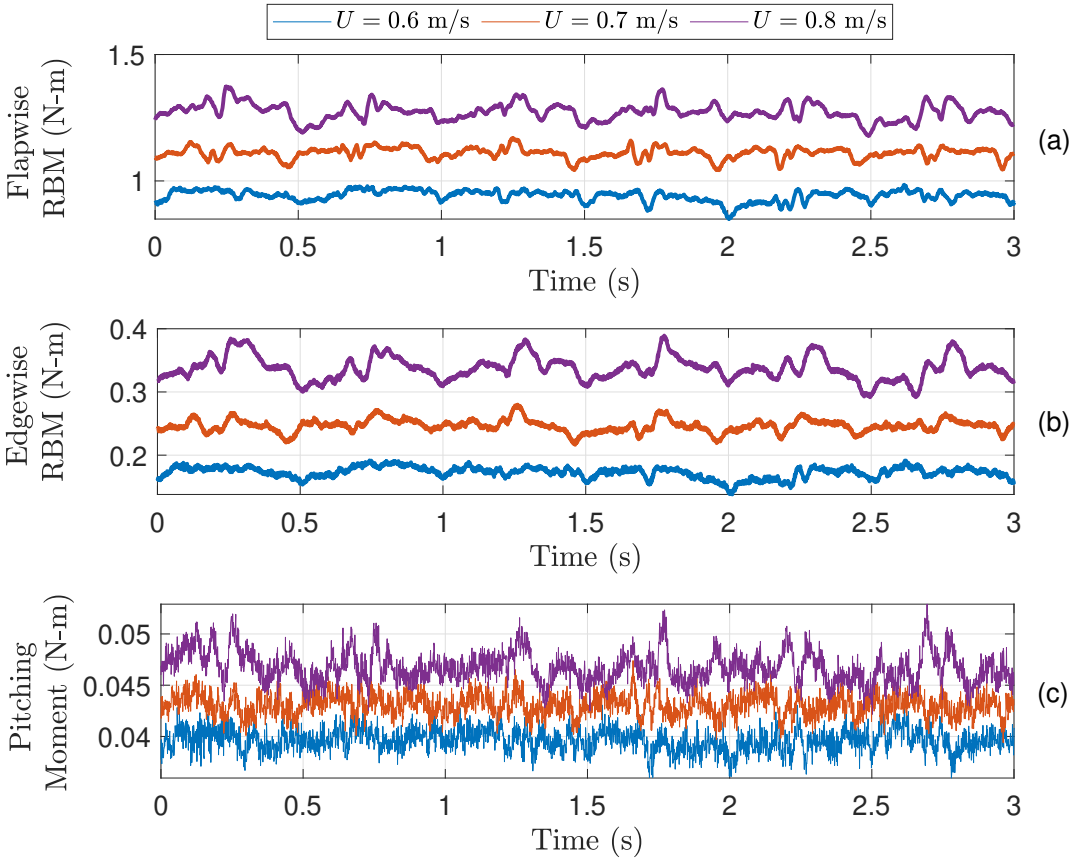


Figure 10: Sample time series of (a) flapwise blade root bending moment, (b) edgewise blade root bending moment, and (c) pitching moment when operating at a rotation rate of 2 rps.

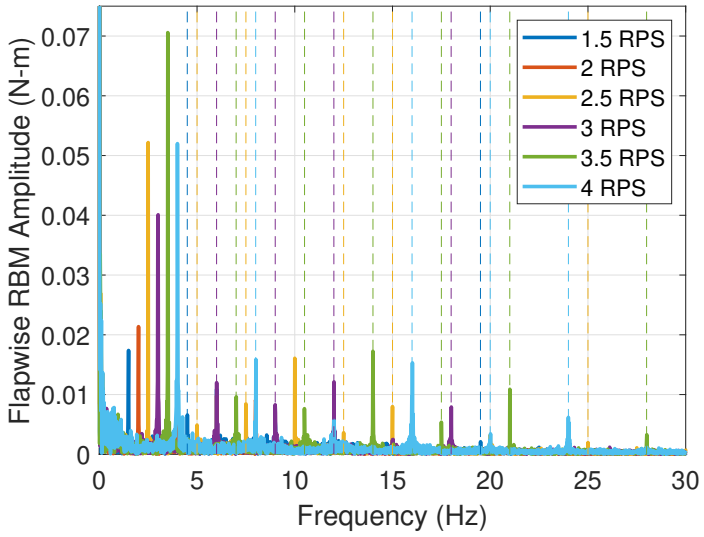


Figure 11: Flapwise blade root bending moment in frequency space. Dashed lines indicate an integer multiple of the rotation rate. Inflow speed is 0.8 m/s.

# 5 Acknowledgements

This work was funded through the National Renewable Energy Laboratory by the Powering the Blue Economy initiative sponsored by the Department of Energy's Water Power Technologies Office.

# References


[1] A. Copping et al. "Maritime renewable energy markets: Power from the sea". In: *Maritime Technology Society Journal* 52.5 (2018), pp. 99–109.

[2] Z. Zhou et al. "Developments in large marine current turbine technologies - a review". In: *Renewable and Sustainable Energy Reviews* 71 (2017), pp. 852–858.

[3] S. Walker and P.R. Thies. "A review of component and system reliability in tidal turbine deployments". In: *Renewable and Sustainable Energy Reviews* 151 (2021). DOI: 10.1016/j.rser.2021.111495.

[4] P. Qian et al. "Review on configuration and control methods of tidal current turbines". In: *Renewable and Sustainable Energy Reviews* 108 (2019), pp. 125–139. DOI: 10.1016/j.rser.2019.03.051.

[5] C.L. Bottasso et al. "Optimization-based study of bend–twist coupled rotor blades for passive and integrated passive/active load alleviation". In: *Wind Energy* 16.8 (2013), pp. 1149–1166.

[6] S.M. Barr and J.W. Jaworksi. "Optimization of tow-steered composite wind turbine blades for static aeroelastic performance". In: *Renewable Energy* 139 (2019), pp. 859–872. DOI: 10.1016/j.renene.2019.02.125.

[7] J.N. Tamayo-Avendaño et al. "Fluid–structure interaction analysis of a wind turbine blade with passive control by bend–twist coupling". In: *Advanced Structural Response and Performance of Wind Turbines* 16 (2023). DOI: 10.3390/en16186619.

[8] R.E. Murray et al. "Passively adaptive tidal turbine blades: design tool development and initial verification". In: *International Journal of Marine Energy* 14 (2016), pp. 101–114.

[9] M.R. Motley and R. Barber. "Passive control of marine hydrokinetic turbine blades". In: *Composite Structures* 110 (2014), pp. 133–139.

[10] R.F. Nicholls-Lee, S.R. Turnock, and S.W. Boyd. "Application of bend–twist coupled blades for horizontal axis tidal turbines". In: *Renewable Energy* 50 (2013), pp. 541–550.

[11] Y.L. Young et al. "Adaptive composite marine propulsors and turbines: progress and challenges". In: *Applied Mechanics Review* 68.6 (2016). DOI: 10.1115/1.4034659.

[12] K.D. Van Ness et al. "Experimental comparison of speed and pitch control strategies for horizontal-axis current turbines". In: *Journal of Ocean Engineering and Marine Energy* 7 (2020), pp. 83–96.

[13] K.D. Van Ness, A. Aliseda, and B.L. Polagye. "Experimental comparison of passive adaptive blade pitch control strategies for an axial-flow current turbine". In: *Journal of Ocean Engineering and Marine Energy* 10 (2023), pp. 105–123.

[14] H. Ross and B. Polagye. "An experimental assessment of analytical blockage corrections for turbines". In: *Renewable Energy* 152 (2020), pp. 1328–1341.

[15] X. Filler. *Hexcel Product Data Sheet: HexTow AS4 Carbon Fiber*. Tech. rep. CTA311 AG23. Hexcel, 2023.

[16] K. Martlett. *Hexcel 8552 IM7 Unidirectional Prepreg 190 gsm & 35%RC Qualification Material Property Data Report*. Tech. rep. NCAMP Test Report Number: CAM-RP-2009-015 REV A. National Institue for Aviation Research, 2011.

[17] F. Zilic de Arcos, C.R. Vogel, and H.J. Willden. "Hydrodynamic independence and passive control application of twist and flapwise deformations of tidal turbine blades". In: *Journal of Fluids and Structures* 118 (2023). DOI: 10.1016/j.jfluidstructs.2022.103827.

[18] H. Wada et al. "Deformation evaluation of elastic composite blade models for a tidal power generation by fluid-structure interaction analysis". In: *Proceedings of the 18th International Conference on Composite Materials*. Jeju, Korea, Aug. 2011.